

---

# An Unsupervised Information-Theoretic Perceptual Quality Metric

---

**Sangnie Bhardwaj**  
Google Research  
sangnie@google.com

**Ian Fischer**  
Google Research  
iansf@google.com

**Johannes Ballé**  
Google Research  
jballe@google.com

**Troy Chinen**  
Google Research  
tchinen@google.com

## Abstract

Tractable models of human perception have proved to be challenging to build. Hand-designed models such as MS-SSIM remain popular predictors of human image quality judgements due to their simplicity and speed. Recent modern deep learning approaches can perform better, but they rely on supervised data which can be costly to gather: large sets of class labels such as ImageNet, image quality ratings, or both. We combine recent advances in information-theoretic objective functions with a computational architecture informed by the physiology of the human visual system and unsupervised training on pairs of video frames, yielding our Perceptual Information Metric (PIM). We show that PIM is competitive with supervised metrics on the recent and challenging BAPPS image quality assessment dataset. We also perform qualitative experiments using the ImageNet-C dataset, and establish that our approach is robust with respect to architectural details.

## 1 Introduction

Many vision tasks require the assessment of subjective image quality for evaluation, including compression and restoration problems such as denoising, deblurring, colorization, etc. The success of many such techniques is measured in how similar the reconstructed image appears to human observers, compared to the often unobserved original image (the image before compression is applied, the actual scene luminances without the noise of the sensor, etc.). Predicting subjective image quality judgements is a difficult problem.

So far, the field has been dominated by simple models with few parameters that are hand-adjusted to correlate well with human mean opinion scores (MOS), such as SSIM and variants [32, 31]. This class of models captures well-documented phenomena observed in visual psychology, such as spatial frequency dependent contrast sensitivity [29], or are based on models of early sensory neurons, such as divisive normalization, which explains luminance and/or contrast adaptivity [16]. It is remarkable these models perform as well as they do given their simplicity. However, it is also clear that these models can be improved upon by modeling more complex and, at this point, potentially less well understood properties of human visual perception. Examples for this can be found in the recent literature [36, 7]. The underlying hypothesis in these models is that the same image features extracted for image classification are also useful for other tasks, including prediction of human image quality judgements. However, this approach requires model fitting in several stages, as well as data collected from human raters for training the models. First, human responses are collected on a large-scale classification task, such as the ImageNet dataset [25]. Second, a classifier network is trained to predict human classifications. Third, more human responses are collected on an image

quality assessment (IQA) task. Fourth, the features learned by the classifier network are frozen and augmented with additional processing stages that are fitted to predict the human IQA ratings. This process is cumbersome, and gathering human responses is costly and slow.

In this paper, we follow a different, and potentially complementary approach. Our work is inspired by two principles that have been hypothesized to shape sensory processing in biological systems. One goes back to as early as the 1950s: the idea of *efficient coding* [2, 3]. The efficient coding hypothesis proposes that the internal representation of images in the human visual system is optimized to efficiently represent the visual information processed by it. That is, the brain *compresses* visual information. The other principle is *slowness* [14, 21, 34], which posits that image features that are not persistent across small time scales are likely to be uninformative for human decision making. For example, two images taken of the same scene within a short time interval would in most cases differ in small ways (e.g., by small object movements, different instances of sensor noise, small changes in lighting), but informative features, such as object identity, would persist. The concept of slowness is related to the information theoretic quantity of *predictive information* [5], which we define here as the mutual information between the two images. In this view, the information that is not predictive is likely not perceived, or at least does not significantly contribute to perceptual decision making.

We conjecture that by constructing a metric based on an image representation that efficiently encodes temporally persistent visual information we will be able to make better predictions about human visual perception. We find that this metric is competitive with the fully supervised LPIPS model [36] on the triplet human rating dataset published in the same paper (BAPPS-2AFC), and outperforms the same model on the corresponding just-noticeable-difference dataset (BAPPS-JND). Remarkably, our model achieves this without requiring any responses collected from humans whatsoever.

## 2 Perceptual Information Metric

A principled approach to defining an IQA metric is to construct an image representation, for example, by transforming the image via a deterministic function into an alternate space, and then measuring distances in this space. Thresholding the distance between two image representations can be used to make predictions about the just-noticeable difference (JND) of image distortions; comparing the distance between two alternate image representations and a reference representation can be used to make predictions about which of the alternate images appears more similar to the reference. The model of Laparra et al. [20] is a recent example of this approach.

More generally, we can construct a probabilistic representation by representing an image as a probability distribution over a latent space. This gives the model flexibility to express uncertainty, such as when image content is ambiguous. Here, we construct a multi-scale probabilistic representation  $q(Z|X)$ , where  $X$  is an image, and  $Z$  is a random variable defined on a collection of multi-scale tensors. The encoder distribution  $q$  is parameterized by artificial neural networks (ANNs) taking images as inputs (Figs. 1 and 2), which allows amortized inference (i.e., the latent-space distribution can be computed in constant time). To use this representation as an IQA metric, we measure simple Euclidean distances between the conditional expected value of  $q$  given different images, i.e.  $\|\mathbb{E} q(Z|X) - \mathbb{E} q(Z|Y)\|_2$ , which gives rise to our Perceptual Information Metric (PIM).

To train this representation unsupervisedly, we are guided by a number of inductive biases, described in the following sections. Note that implementation details regarding the optimization (e.g. optimization algorithm, learning rate) and pre-processing of the training dataset can be found in the appendix.

### 2.1 Choice of objective function

Our choice of objective function is informed by both the efficient coding and the slowness principles: it must be compressive, and it must capture temporally persistent information. We choose a stochastic variational bound on the Multivariate Mutual Information (MMI) to satisfy these constraints, called IXYZ [12]. IXYZ learns a stochastic representation,  $Z$ , of two observed variables,  $X$  and  $Y$  (in this case two temporally close images of the same scene), such that  $Z$  maximizes a lower bound on the Multivariate Mutual Information (MMI),  $I(X; Y; Z)$ :

$$I(X; Y; Z) = H(Z) - H(Z|X) - H(Z|Y) + H(Z|X, Y) \quad (1)$$

$$= \int dx dy p(x, y) \int dz p(z|x, y) \log \frac{p(z|x)p(z|y)}{p(z)p(z|x, y)} \quad (2)$$

$$= \mathbb{E}_{x,y,z} \log \frac{p(z|x)p(z|y)}{p(z)p(z|x,y)} \geq \mathbb{E}_{x,y,z} \log \frac{q(z|x)q(z|y)}{\hat{p}(z)p(z|x,y)} \equiv \text{IXYZ} \quad (3)$$

Here,  $p(z|x, y)$  is our *full encoder* of the pair of images, and  $q(z|x)$  and  $q(z|y)$  are variational approximations to the encoders of  $X$  and  $Y$ , which we call *marginal encoders*, since they must learn to marginalize out the missing conditioning variable (e.g.,  $y$  is the marginalization variable for  $q(z|x)$ ). All three of those can be parameterized by the outputs of neural networks.  $\hat{p}(z)$  is a minibatch marginalization of  $p(z|x, y)$ :  $\hat{p}(z) \equiv \frac{1}{K} \sum_{i=1}^K p(z|x_i, y_i)$ , where  $K$  is the number of examples in the minibatch.<sup>1</sup> With those three substitutions, IXYZ is a lower bound that we can maximize using stochastic gradient descent.

As described in Fischer [12], this objective is compressive. It can be written as:

$$I(X; Y; Z) = I(Z; X, Y) - I(X; Z|Y) - I(Y; Z|X) \geq \text{IXYZ} \quad (4)$$

Thus, when we maximize IXYZ, we are directly compressing out irrelevant information about  $X$  for predicting  $Y$  with the  $I(X; Z|Y)$  term, and irrelevant information about  $Y$  for predicting  $X$  with the  $I(Y; Z|X)$  term.

## 2.2 Parameterization of encoder distributions

As stated above, we seek a distribution over the representation conditioned on an image; hence, the marginal encoder  $q(z|x)$  is the core piece we are trying to learn. The full encoder  $p(z|x, y)$  is only necessary for training, and it is the only distribution we need to sample from. We are able to use mixture distributions for the marginal encoders, since we don't need to sample from them, but only need to take gradients through their log probability functions. This is a benefit of IXYZ compared to other variational approaches like the Variational Information Bottleneck (VIB) [1] or the Conditional Entropy Bottleneck [13].<sup>2</sup>

Using mixture distributions for  $q(z|x)$  allows us to learn very expressive inference encoders that, in the limit of infinite mixtures, can exactly marginalize the full encoder distribution,  $p(z|x, y)$ . In practice, infinite mixtures is too many, but we find that even just a mixture of ten Gaussians for  $q(z|x)$  and  $q(z|y)$  is sufficient to learn powerful models with tight upper bounds on the compression terms in our experiments.

For the full encoder, we parameterize only the mean of a multivariate Gaussian, setting the variance to one. This ensures that the latent space is Euclidean, thereby making it appropriate for use as a metric. Correspondingly, the marginal encoders are mixtures of multivariate Gaussians, also with unit variance for each mixture component.

## 2.3 Choice of dataset

In line with the slowness principle, we seek to extract the predictive information of two images  $X$  and  $Y$  taken within short time intervals. We approximate this by extracting pairs of consecutive frames from video sequences, 1/30th of a second apart, which is generally short enough to simulate continuous motion to the human visual system (HVS). The nature of the imagery used for training can of course vary according to video content. For example, the statistics of horizontal and vertical edges, as well as the amount of and type of texture tends to differ between motifs, e.g., in city scenes vs. nature scenes. Importantly, image composition can have an effect on the distribution of object scales. Natural visual environments tend to exhibit *scale invariance*: both the statistics of images recorded by photographers as well as the properties of feature detectors in the early human visual system themselves are self-similar across scales, such as the neurons found in cortical region V1 [11]. Our training data is largely determined by its availability: we leveraged the database of publicly available videos on YouTube. In our experiments, we were forced to reduce the spatial resolution of the video to eliminate existing compression artifacts, which limits the expression of scale invariance in the training dataset. We addressed this issue by imposing approximate scale invariance on the computational architecture described in the next section.

<sup>1</sup>See Fischer [12] and Poole et al. [24] for detailed descriptions of the minibatch marginal distribution.

<sup>2</sup>In contrast, VIB uses the same encoder for both training and inference, which means that the encoder distribution cannot be a discrete mixture, since sampling the distribution during training would require taking gradients through the discrete sample.

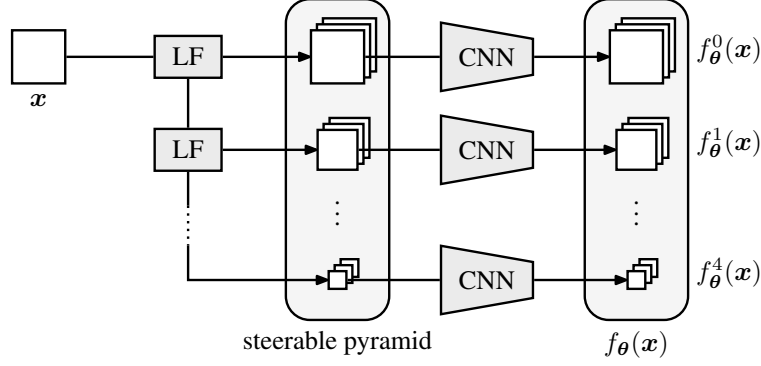


Figure 1: System diagram of frontend shared between all encoders. An image ( $x$ ) is decomposed using linear filtering (LF) into a multi-scale pyramid representation. Each scale is then subjected to processing by a convolutional neural network (CNN) with trained parameters  $\theta$ , which are not shared across scales. The result is a multi-scale collection of tensors we denote  $f_{\theta}(x)$ .

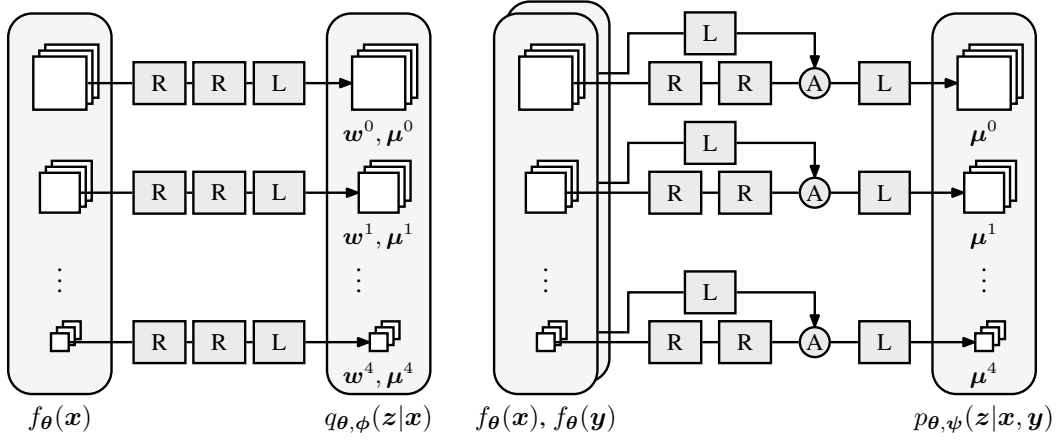


Figure 2: **Left:** system diagram of marginal encoder  $q_{\theta,\phi}(z|x)$  (identical for  $q_{\theta,\phi}(z|y)$ ). Each tensor produced by the frontend is fed into a three-layer neural network consisting of two rectified linear layers (R) with 100 units each, and one linear layer (L), which outputs 10 mixture weights and 10 mean vectors of length 10 per spatial location and scale. The parameters of both marginal encoders are identical, not shared across scales, and denoted together as  $\phi$ . **Right:** system diagram of full encoder  $p_{\theta,\psi}(z|x,y)$ , whose parameters we denote as  $\psi$ . Each tensor of  $f_{\theta}(x)$  is fed into a three-layer network with 10 units per layer, the final outputs representing one mean vector per spatial location and scale.  $f_{\theta}(y)$  is subjected to a linear layer, which outputs 10 factors and 10 offsets of an additional elementwise affine transformation (A) of the activations of the second layer (R). All layers are separable in space, i.e. convolutions with  $1 \times 1$  spatial support.

## 2.4 Choice of architectural components

As we specify the model details, we now indicate learned parameters with Greek subscripts, and vectors with bold. The mean parameters of the multivariate Gaussians and the mixture weights of the marginal encoders are computed by a multi-stage architecture of ANNs, as shown in Figs. 1 and 2. All encoder distributions are defined jointly on a collection of multi-scale latent variables (i.e.,  $z = \{z^0, \dots, z^4\}$ ), but the distribution parameters (means, and mixture weights for the marginal encoders) are computed independently for each scale. Each  $z^s$  has 10 dimensions per spatial location.

All three encoders share the same computational frontend with parameters  $\theta$ , which we denote  $f_{\theta}(x)$ . This frontend, shown in Fig. 1, consists of a multi-scale transform with no trainable parameters, followed by a set of convolutional neural networks (CNNs). We use a steerable pyramid [26] with 3 bandpass scales. Each bandpass scale has 2 oriented subbands, making for 8 sub-bands per color channel total, including the highpass and lowpass residuals. Note that the spatial resolution of the

scales varies as defined by the multi-scale pyramid. The CNNs each consist of 4 layers with 64, 64, 256 and 3 units, respectively, a spatial support of  $5 \times 5$ , and ReLU activation function.

The marginal encoder takes the output of the frontend as its input, and outputs the conditional mean vectors and weights of a 10-dimensional Gaussian mixture distribution with 10 unit-variance mixture components (Fig. 2, left panel) per spatial location and scale. The marginal encoders for  $X$  and  $Y$  are identical, i.e. share all parameters. The full encoder takes the output of the frontend to both  $\mathbf{x}$  and  $\mathbf{y}$ , and computes the conditional mean via a separate set of neural networks (Fig. 2, right panel).

The architectural inductive bias can thus be summarized in three constraints: *spatial translation invariance* via the convolutionality of all components of the architecture; *approximate spatial scale invariance*, by separating the image representation into multiple scales and forcing the computation to be independent across scales (effectively forcing the model to equally weight information from each of the scales, although it does not explicitly assume scale invariance of the computation); and *temporal translation invariance* by sharing parameters between the marginal encoders.

### 3 Evaluation

We assess the properties of our unsupervised representation in four ways. First, we use PIM to make predictions on a dataset of human image quality ratings, previously collected under a two-alternative forced choice (2AFC) paradigm, comparing it to other recently proposed metrics on this task. Second, we posit that shifting an image by a small number of pixels should only have negligible effect on human perceptual decision making. We quantify this on PIM and a variety of metrics. Third, we generalize this experiment to gather intuitions about the relative weighting of different types of distortions via the ImageNet-C dataset [17]. Finally, we assess the robustness of our approach using a number of ablation experiments.

#### 3.1 Performance on BAPPS

We evaluate the performance of PIM on BAPPS, a dataset of human perceptual similarity judgements [36]. BAPPS contains two task-specific datasets: a triplet dataset, in which humans were asked to identify the more similar of two distorted images compared to a reference image, named “2AFC”, and a dataset of image pairs judged as identical or not, named “JND”. For reporting the performance of PIM, we follow the original authors: for BAPPS-2AFC, we report the fraction of human raters agreeing with the metric as a percentage. For BAPPS-JND, we report mAP, an area-under-the-curve score.

We compare PIM to two traditional perceptual quality metrics, MS-SSIM and NLPD, and the more recent LPIPS, published with the BAPPS dataset. For LPIPS, we use the two models provided by the authors: LPIPS Alex, which uses AlexNet to extract features, and LPIPS Alex-lin, which also uses a linear network on top of the features of pretrained AlexNet.

Results and comparison with these other metrics are summarized in Table 1. The numbers reported for PIM are the best out of 10 repeats. PIM scores  $69.33 \pm 0.04\%$  on 2AFC and  $63.49 \pm 0.14\%$  on BAPPS-JND on average across the 10 runs. The best model at 63.69% performs the best out of all metrics on BAPPS-JND, outperforming both LPIPS Alex and Alex-lin. On BAPPS-2AFC, it scores 69.40%, outperforming LPIPS Alex and performing at about the same level as Alex-lin. We reiterate that Alex and Alex-lin use ImageNet labels during training of the base model, and Alex-lin additionally trains on human ratings, while PIM does not train with any labels or ratings.

#### 3.2 Invariance under pixel shifts

Metrics such as MS-SSIM and NLPD, which operate on pairwise comparisons between corresponding spatial locations in images, typically do not perform well on geometric transformations (and older benchmarks often do not contain this type of distortion). More complex metrics such as LPIPS and PIM should perform better. To verify this, we follow the approach of Ding et al. [9] and shift the reference images in BAPPS by a few pixels ( $\leq 5$  for a 64x64 image). Because the shifts are very small, we can reasonably assume that human judgements of the modified pairs would be essentially unchanged.

The score differences w.r.t. the unmodified BAPPS results on this transformed dataset are presented in

Table 1: Scores on BAPPS. Best values are underlined, the bold values are within 0.5% of the best. All numbers reported for LPIPS were computed using the code and weights provided by Zhang et al. [36]. Categories follow the same publication and “all” indicates overall scores.

Metric	BAPPS-2AFC						BAPPS-JND			
	Trad.	CNN	SuperRes	Deblur	Coloriz.	Interp.	All	Trad.	CNN	All
MS-SSIM	61.24	79.34	64.62	58.88	57.28	57.29	63.26	36.20	63.77	52.50
NLPD	58.23	80.29	65.54	58.83	60.07	55.40	63.50	34.91	61.49	50.80
LPIPS Alex	71.91	<b>83.55</b>	<b>71.57</b>	60.45	64.94	62.74	68.98	46.88	67.86	59.47
LPIPS Alex-lin	75.27	<b>83.52</b>	<b>71.11</b>	<b>61.17</b>	<b>65.17</b>	<b>63.35</b>	<b>69.53</b>	51.92	67.78	61.50
PIM	<b>75.85</b>	83.01	<b>71.55</b>	<b>61.29</b>	63.25	62.67	<b>69.41</b>	<b>57.90</b>	<b>68.45</b>	<b>63.69</b>

Table 2: Score differences on pixel-shifted BAPPS. Bold values indicate best for a column.

Metric \ Shift	BAPPS-2AFC					BAPPS-JND				
	1	2	3	4	5	1	2	3	4	5
MS-SSIM	-1.18	-7.62	-11.10	-12.70	-13.50	-11.60	-17.60	-19.98	-21.20	-21.80
NLPD	-2.18	-7.22	-10.40	-12.40	-13.80	-13.20	-18.10	-19.99	-20.70	-21.00
LPIPS Alex	-0.06	-0.25	-0.34	-0.48	-0.68	-3.90	-6.96	-8.64	-9.77	-11.50
LPIPS Alex-lin	-0.11	-0.18	-0.27	<b>-0.30</b>	<b>-0.48</b>	-1.99	-3.34	-4.56	-5.49	-7.06
PIM	<b>-0.02</b>	<b>-0.08</b>	<b>-0.19</b>	-0.42	-0.64	<b>-0.01</b>	<b>-0.77</b>	<b>-2.57</b>	<b>-4.68</b>	<b>-6.77</b>

Table 2. MS-SSIM and NLPD lose over 7 percentage points on BAPPS-2AFC when shifting by only 2 pixels, while the deep metrics (including PIM) have only a negligible decrease. On BAPPS-JND the effect is even more stark, where both traditional metrics’ scores decrease by almost 12 when shifting by 1 pixel, and 18 for 2 pixels. LPIPS’ scores show a more noticeable decrease on shifting by 2 pixels as well, 7 for LPIPS Alex and 3 for LPIPS Alex-lin. PIM performance decreases by less than one.

### 3.3 Qualitative comparisons via ImageNet-C

Hendrycks and Dietterich [17] provide a dataset, ImageNet-C, which consists of 15 corruption types with 5 different severity levels applied to the ImageNet validation set, meant as a way to assess classifiers. We compared the predictions PIM, LPIPS and MS-SSIM make with respect to the various types of corruptions subjectively; we also added two additional corruptions, pixel shift and zoom, also with 5 levels of severity. We observed two significant effects across the dataset: First, MS-SSIM deviates from the other metrics on geometric distortions such as zoom, shift, and “elastic transform”, further giving weight to the observations made in the previous section. Second, we noted that LPIPS deviates from PIM and MS-SSIM on global changes of contrast and similar distortions such as “fog”. Subjectively, we found that LPIPS was not sensitive enough to this kind of corruption. We speculate this may be due to LPIPS using pre-trained features from a classifier network, which in principle should be invariant to global changes in lighting. Indeed, it is plausible that the invariances of a model predicting image quality should not necessarily be identical to the invariances of a network solving a classification task.

To quantify these effects, we conducted the following simple experiment: For a given metric, we computed the metric value between a reference and a corrupted image and then found an equivalent amount of Gaussian noise to add to the reference that yields the same metric value. We plotted the average standard deviation of required Gaussian noise across the dataset in Fig. 3(a). Clearly, MS-SSIM is more sensitive to the “zoom” corruption than the other metrics, and LPIPS is less sensitive to “fog” than MS-SSIM and PIM, both relative to their sensitivity to Gaussian noise. Fig. 3(b) and (c) show the corresponding noise strengths for a representative image. It is interesting to note that the images corrupted by fog are distinguishable at a glance, even at the lowest corruption strength. However, they remain recognizable (i.e. classifiable), suggesting that a classifier, which LPIPS is based on, should be invariant to the corruption.

Further details of this experiment can be found in the appendix. Note that these results are not necessarily conclusive, and more sophisticated experiments are needed to assess the different classes

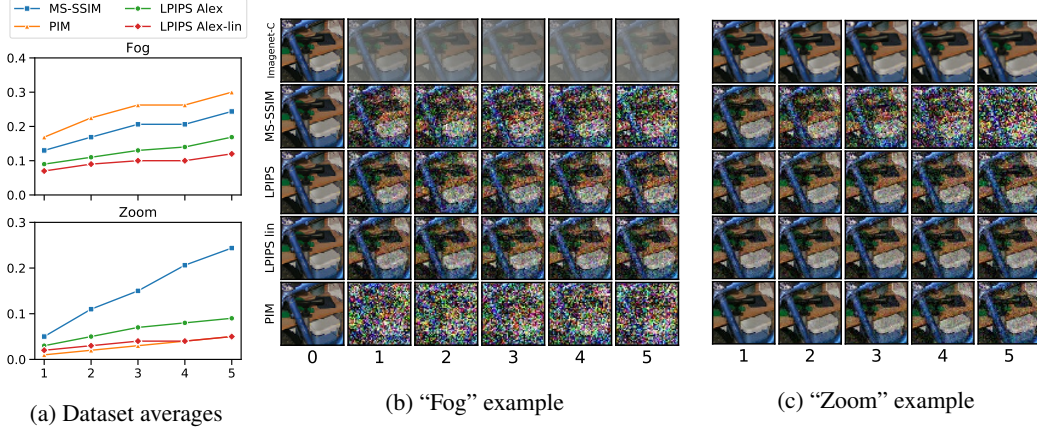


Figure 3: (a): standard deviation of Gaussian noise added to images on average to yield the same metric value as the given corruption strength. (b) and (c): Each column shows equivalent amount of Gaussian noise to the corruption in the first row, according to the metric.

of metrics, such as with the methods presented by Wang and Simoncelli [30] or Berardino et al. [4]. These would go beyond the scope of this paper.

### 3.4 Ablations

To study the effect of the different inductive biases we impose, specifically the loss, the use of a multi-scale architecture, and the training technique and dataset, we conduct ablation experiments detailed below.

**Alternate objective functions.** We compare the IXYZ objective to two other information theoretic objectives: *InfoNCE* and *Single variable InfoNCE* [22, 24]. InfoNCE is a lower bound on  $I(X; Y)$  that uses the same form of minibatch marginal as IXYZ. We can write InfoNCE as  $I(X; Y) \geq I(Y; Z) \geq \mathbb{E}_{\mathbf{x}, \mathbf{y}, \mathbf{z} \sim p(\mathbf{x}, \mathbf{y}) q_{\theta, \phi}(\mathbf{z} | \mathbf{x})} \log \frac{q_{\theta, \phi}(\mathbf{z} | \mathbf{y})}{\frac{1}{K} \sum_{i=1}^K q_{\theta, \phi}(\mathbf{z} | \mathbf{y}_i)}$ . Single variable InfoNCE<sup>3</sup> also uses a minibatch marginal and can be written as  $I(X; Z) \geq \mathbb{E}_{\mathbf{x}, \mathbf{z} \sim p(\mathbf{x}) q_{\theta, \phi}(\mathbf{z} | \mathbf{x})} \log \frac{q_{\theta, \phi}(\mathbf{z} | \mathbf{x})}{\frac{1}{K} \sum_{i=1}^K q_{\theta, \phi}(\mathbf{z} | \mathbf{x}_i)}$ . The primary difference between InfoNCE and IXYZ is that InfoNCE is not explicitly compressive. The learned representation,  $Z$ , is not constrained to only capture information shared between both  $X$  and  $Y$ . Single variable InfoNCE is even less constrained, since  $Z$  just needs to learn to distinguish between images ( $X$ ) that are independently sampled in the minibatch, whereas InfoNCE and IXYZ have to be able to use  $Z$  to select the correct  $Y$  for the observed  $X$ .

Training the PIM architecture using InfoNCE gives 68.9% and 62.5% on 2AFC and JND respectively, whereas single variable InfoNCE gives 64.5% and 44.79%. This shows that losing the compression and slow feature aspects of the IXYZ objective result in weaker performance for the PIM architecture.

**No multi-scale decomposition.** We trained a number of models analogous to PIM, but without enforcing approximate scale invariance: omitting the frontend multiscale pyramid, and with only one CNN, either using only its outputs or its outputs as well as hidden layer activations in place of  $f_{\theta}(\mathbf{x})$ . For this we chose two networks used in LPIPS, VGG16 [27] and AlexNet [19], and the 4-layer CNN used in the frontend of PIM. Figure 4 (left) shows that none of these experiments achieved a performance close to PIM. Imposing scale invariance thus leads to better predictions. We also note that VGG and AlexNet perform worse than the 4-layer CNN, which has much fewer parameters.

**Alternate multi-scale/CNN architectures.** We considered the Laplacian pyramid [6] as an alternative linear multi-scale decomposition, and multiple alternative CNN architectures for the frontend. Specifically, we compare against VGG16, AlexNet, and shallower variations of the 4-layer deep convolutional network that PIM uses. The results in Fig. 4 (right) show that of all these choices, the PIM architecture gives the best results, but nonetheless the others still do reasonably well. The approach thus is robust with respect to architectural details.

<sup>3</sup>This bound is called "InfoNCE with a tractable conditional" in Poole et al. [24].

CNN	2AFC	JND	Pyramid	CNN	2AFC	JND
4-layer	66.2	54.08	Laplacian	VGG16	67.4	63.8
AlexNet	58.13	37.78	Laplacian	2-layer	68.4	61.6
VGG16	59.74	39.76	Laplacian	3-layer	68.7	61.9
AlexNet (+ hidden layers)	62.73	47.81	Laplacian	4-layer	68.6	61.2
VGG16 (+ hidden layers)	67.59	61.35	Steerable	VGG16	67.9	60.1
			Steerable	2-layer	68.8	60.9
			Steerable	3-layer	69.2	63.2
			<b>Steerable</b>	<b>4-layer</b>	<b>69.4</b>	<b>63.69</b>

Figure 4: Left: BAPPS performance for various CNN architectures without using a frontend multi-scale decomposition. “+ hidden layers” indicates that the hidden layer activations were used as part of the representation (in place of the multi-scale tensors of  $f_{\theta}(x)$ ). Right: BAPPS performance of our approach with alternate architectural choices. Bold indicates the choice used in PIM.

## 4 Related work

Early IQA metrics were based strictly on few hand-tunable parameters and architectural inductive biases informed by observations in visual psychology and/or computational models of early sensory neurons [e.g., 33, 28]. SSIM and its variants, perhaps the most popular descendant of this class [32, 31], define a quality index based on luminance, structure and contrast changes as multiplicative factors. FSIM [35] weights edge distortions by a bottom-up saliency measure. PSNR-HVS and variant metrics explicitly model contrast sensitivity and frequency masking [10, 23].

Another member of this class of metrics, the Normalized Laplacian Pyramid Distance [NLPD; 20] has more similarities to our approach, in that an architectural bias – a multi-scale pyramid with divisive normalization – is imposed, and the parameters of the model (<100, much fewer than PIM) are fitted unsupervisedly to a dataset of natural images. However, the authors use a spatially predictive loss function, which is not explicitly information theoretic. While the model is demonstrated to reduce redundancy in the representation (i.e. implements efficient coding), it does not exploit temporal learning.

More recently, deep representations emerged from the style transfer literature, where pre-trained classifier features are used as an image embedding [15]. Zhang et al. [36] and Chinen et al. [7] trained models using IQA-specific datasets on such VGG-based representations. Ding et al. [8] refined this by computing an SSIM-like measure on a VGG representation. As discussed earlier, these representations require collecting human responses, as well as pre-training on other tasks such as classification, that are otherwise unrelated to IQA.

To our knowledge, PIM is the first IQA metric that explicitly uses the slowness principle as an inductive bias.

## 5 Conclusion

In this paper, we demonstrate that making accurate predictions of human image quality judgements does not require a model that is supervisedly trained. Our model is competitive with or exceeds the performance of a recent supervised model [36], while only relying on a few essential ingredients: a dataset of natural videos; a compressive objective function employed to extract temporally persistent information from the data; a distributional parameterization that is flexible enough to express uncertainty; a computational architecture that imposes spatial scale invariance, as well as spatial and temporal translation invariance.

Our model is consistent with the *efficient coding* and *slowness* principles formulated in computational neuroscience, and we demonstrate that our basic approach is not overly dependent on the implementation details of the computational architecture, such as the multi-scale transform or the precise neural network architecture. Instead, it is robust with respect to changes in the architecture that do not fundamentally alter the ingredients mentioned above.

## Broader Impact

Many deep perceptual image metrics rely on the collection of large datasets of rated images as training data; such data could reflect the biases of human raters. While we cannot claim that PIM is free of bias, by being completely unsupervised, one possible source of bias is removed.

The broad concern about AI reducing work opportunities, in this case, seems inapplicable. Perceptual metrics are most often used as loss functions in the development of some other product, but the final quality ultimately needs to be verified by human eye. We envision this need for verification continuing into the foreseeable future.

On the other hand, good perceptual metrics have the potential to enable other research and technology which improves the lives of AI consumers, as well as reduce the burden on researchers of frequent, tiresome – and often infeasible at scale – human evaluations.

## References

- [1] Alexander A. Alemi et al. “Deep Variational Information Bottleneck”. In: *Proc. of 5th Int. Conf. on Learning Representations*. 2017. URL: <https://openreview.net/forum?id=HyxQzBceg>.
- [2] Fred Attneave. “Some Informational Aspects of Visual Perception”. In: *Psychological Review* 61.3 (1954). DOI: 10.1037/h0054663.
- [3] Horace B. Barlow. “Possible Principles Underlying the Transformations of Sensory Messages”. In: *Sensory Communication. Contributions to the Symposium on Principles of Sensory Communication*. M.I.T. Press, 1961, pp. 217–234. ISBN: 978-0-262-51842-0.
- [4] Alex Berardino et al. “Eigen-Distortions of Hierarchical Representations”. In: *Advances in Neural Information Processing Systems* 30. 2017.
- [5] William Bialek, Ilya Nemenman, and Naftali Tishby. “Predictability, complexity, and learning”. In: *Neural Computation* 13.11 (2001). DOI: 10.1162/089976601753195969.
- [6] Peter J. Burt and Edward H. Adelson. “The Laplacian Pyramid as a Compact Image Code”. In: *IEEE Transactions on Communications* 31.4 (Apr. 1983). DOI: 10.1109/TCOM.1983.1095851.
- [7] Troy Chinen et al. “Towards a Semantic Perceptual Image Metric”. In: *2018 25th IEEE International Conference on Image Processing (ICIP)*. 2018. DOI: 10.1109/ICIP.2018.8451611.
- [8] Keyan Ding et al. *Image Quality Assessment: Unifying Structure and Texture Similarity*. cite arxiv:2004.07728. 2020. URL: <http://arxiv.org/abs/2004.07728>.
- [9] Keyan Ding et al. “Image Quality Assessment: Unifying Structure and Texture Similarity”. In: *CoRR* abs/2004.07728 (2020). URL: <https://arxiv.org/abs/2004.07728>.
- [10] Karen O. Egiazarian et al. “A New Full-Reference Quality Metric Based On HVS”. In: *CD-ROM Proceedings of the Second International Workshop on Video Processing and Quality Metrics*. 2006.
- [11] David J. Field. “Relations Between the Statistics of Natural Images and the Response Properties of Cortical Cells”. In: *Journal of the Optical Society of America A* 4.12 (1987). DOI: 10.1364/JOSAA.4.002379.
- [12] Ian Fischer. “Bounding the Multivariate Mutual Information”. In: *Information Theory and Machine Learning Workshop* (2019). URL: [https://drive.google.com/file/d/171JiJ4v\\_6h0p-ist\\_jCrr-o10Di7yELx/view](https://drive.google.com/file/d/171JiJ4v_6h0p-ist_jCrr-o10Di7yELx/view).
- [13] Ian Fischer. “The Conditional Entropy Bottleneck”. In: *arXiv preprint arXiv:2002.05379* (2020).
- [14] Peter Földiák. “Learning Invariance from Transformation Sequences”. In: *Neural Computation* 3.2 (1991). DOI: 10.1162/neco.1991.3.2.194.
- [15] Leon A. Gatys, Alexander S. Ecker, and Matthias Bethge. “Image Style Transfer Using Convolutional Neural Networks”. In: *2016 IEEE Conference on Computer Vision and Pattern Recognition (CVPR)* (2016), pp. 2414–2423.
- [16] David J. Heeger. “Normalization of cell responses in cat striate cortex”. In: *Visual Neuroscience* 9.2 (1992). DOI: 10.1017/S0952523800009640.

- [17] Dan Hendrycks and Thomas Dietterich. “Benchmarking neural network robustness to common corruptions and perturbations”. In: *arXiv preprint arXiv:1903.12261* (2019).
- [18] Diederik P Kingma and Jimmy Ba. “Adam: A method for stochastic optimization”. In: *arXiv preprint arXiv:1412.6980* (2014).
- [19] Alex Krizhevsky, Ilya Sutskever, and Geoffrey E Hinton. “ImageNet Classification with Deep Convolutional Neural Networks”. In: *Advances in Neural Information Processing Systems 25*. Ed. by F. Pereira et al. Curran Associates, Inc., 2012, pp. 1097–1105. URL: <http://papers.nips.cc/paper/4824-imagenet-classification-with-deep-convolutional-neural-networks.pdf>.
- [20] Valero Laparra et al. “Perceptual image quality assessment using a normalized Laplacian pyramid”. In: *Proceedings of SPIE, Human Vision and Electronic Imaging XXI*. 2016. DOI: 10.2352/ISSN.2470-1173.2016.16.HVEI-103.
- [21] Graeme Mitchison. “Removing Time Variation with the Anti-Hebbian Differential Synapse”. In: *Neural Computation* 3.3 (1991). DOI: 10.1162/neco.1991.3.3.312.
- [22] Aaron van den Oord, Yazhe Li, and Oriol Vinyals. “Representation learning with contrastive predictive coding”. In: *arXiv preprint arXiv:1807.03748* (2018).
- [23] Nikolay N. Ponomarenko et al. “On between-coefficient contrast masking of DCT basis functions”. In: *CD-ROM Proc. of the Third International Workshop on Video Processing and Quality Metrics*. 2007.
- [24] Ben Poole et al. “On Variational Bounds of Mutual Information”. In: *ICML2019* (2019). URL: <https://arxiv.org/abs/1905.06922>.
- [25] Olga Russakovsky et al. “ImageNet Large Scale Visual Recognition Challenge”. In: *International Journal of Computer Vision (IJCV)* 115.3 (2015), pp. 211–252. DOI: 10.1007/s11263-015-0816-y.
- [26] Eero P. Simoncelli and William T. Freeman. “The Steerable Pyramid: A Flexible Architecture for Multi-Scale Derivative Computation”. In: *1995 IEEE International Conference on Image Processing (ICIP)*. Vol. 3. 1995. DOI: 10.1109/ICIP.1995.537667.
- [27] Karen Simonyan and Andrew Zisserman. *Very Deep Convolutional Networks for Large-Scale Image Recognition*. 2014. arXiv: 1409.1556 [cs.CV].
- [28] Patrick C. Teo and David J. Heeger. “Perceptual image distortion”. In: *Proc. SPIE 2179, Human Vision, Visual Processing, and Digital Display V*. 1994. DOI: 10.1117/12.172664.
- [29] Floris L. Van Nes and Maarten A. Bouman. “Spatial Modulation Transfer in the Human Eye”. In: *Journal of the Optical Society of America A* 57.3 (1967). DOI: 10.1364/JOSA.57.000401.
- [30] Zhou Wang and Eero P. Simoncelli. “Maximum differentiation (MAD) competition: A methodology for comparing computational models of perceptual quantities”. In: *Journal of Vision* 8.12 (2008). DOI: 10.1167/8.12.8.
- [31] Zhou Wang, Eero P. Simoncelli, and Alan Conrad Bovik. “Multi-Scale Structural Similarity for Image Quality Assessment”. In: *Conf. Rec. of the 37th Asilomar Conf. on Signals, Systems and Computers*. 2003. DOI: 10.1109/ACSSC.2003.1292216.
- [32] Zhou Wang et al. “Image Quality Assessment: From Error Visibility to Structural Similarity”. In: *IEEE Transactions on Image Processing* 13.4 (2004). DOI: 10.1109/TIP.2003.819861.
- [33] A. B. Watson. “DCTune: A Technique for Visual Optimization of DCT Quantization Matrices for Individual Images”. In: *Society for Information Display Digest of Technical Papers* 24 (1993), pp. 946–949.
- [34] Laurenz Wiskott. “Slow Feature Analysis: A Theoretical Analysis of Optimal Free Responses”. In: *Neural Computation* 15.9 (2003). DOI: 10.1162/089976603322297331.
- [35] L. Zhang et al. “FSIM: A Feature Similarity Index for Image Quality Assessment”. In: *IEEE Transactions on Image Processing* 20.8 (Aug. 2011), pp. 2378–2386. ISSN: 1057-7149. DOI: 10.1109/TIP.2011.2109730.
- [36] Richard Zhang et al. “The Unreasonable Effectiveness of Deep Features as a Perceptual Metric”. In: (2018). cite arxiv:1801.03924Comment: Code and data available at <https://www.github.com/richzhang/PerceptualSimilarity>. URL: <http://arxiv.org/abs/1801.03924>.

## A Appendix

### A.1 Training dataset pre-processing

We used 40 000 publicly available videos from YouTube which were available in a spatial resolution of at least  $1920 \times 1080$  pixels. In an attempt not to skew the distribution of content too far from what may inform biological representation learning, we excluded most artificial content such as screenshots and videos of computer games. We decompressed one segment of 30 consecutive frames (corresponding to 1 second) out of each video, yielding a total of ca. 11 hours of training video. To reduce video compression artifacts and prevent systematic downsampling artifacts, each segment was then spatially downsampled to a randomized height between 128 and 160. Each segment was then separated into 15 pairs of neighboring frames, and a randomly placed, but spatially colocated patch of  $64 \times 64$  pixels was cropped out of each frame pair. The order of the frame pairs was then randomized in a running buffer, and all RGB pixel values were normalized to the range between 0 and 1 before being fed into the model.

### A.2 Optimization details

We trained the model on a single GPU with a batch size of 50 for 120 000 steps, which takes about 20 hours. We used the Adam [18] optimizer with an initial learning rate of  $10^{-3}$ , dropping to  $10^{-4}$  after 50 000 and to  $10^{-5}$  after 100 000 steps, respectively. During training, we need to evaluate  $\hat{p}(z)$ , which is  $O(MNB^2)$  in memory for a batch size of  $B$  and a spatial tensor shape of  $M \times N$ . This can exceed the memory of a typical GPU. To resolve this problem, instead of training on the full tensors, we extract  $8 \times 8$  center crops out of all tensors in  $f_\theta(\mathbf{x})$  and  $f_\theta(\mathbf{y})$ . We ensure that the centers of the patches align with each other across the different scales, thus preserving translation invariance.

To train IXYZ models, we use a Lagrange-variant proposed in Fischer [12]:

$$\max_Z (1 - \beta)I(Z; X, Y) - \beta(I(X; Z|Y) + I(Y; Z|X)) \quad (5)$$

$$\geq \max_Z \mathbb{E}_{x,y,z \sim p(x,y)p(z|x,y)} \log \frac{q^\beta(z|x)q^\beta(z|y)}{\hat{p}(z)p^{2\beta-1}(z|x,y)} \quad (6)$$

This technique results in simply maximizing  $I(Z; X, Y)$  when  $\beta = 0$ , but switches to maximizing a lower bound on  $I(X; Y; Z)$  when  $\beta = 1$ . Values of  $\beta$  between 0 and 1 result in increasing compression on the  $I(X; Z|Y)$  and  $I(Y; Z|X)$  terms. We smoothly anneal  $\beta$  from 0 to 1 over the first 10 000 gradient steps to avoid training trivial models where  $Z$  is independent of  $X$  and  $Y$ .

Following the methodology in Zhang et al. [36], we did not select our final model based on a separate validation set, but simply by comparing results on the test set. Given our careful ablation experiments, and the fact that our model is only specified using inductive bias and is trained without supervision, we believe that the risk of overfitting to the test set is minimal.

### A.3 Details and further results on ImageNet-C experiments

To find an equivalent level of Gaussian noise which produces a metric value corresponding to a given corruption, we simply added Gaussian noise with a range of levels to the uncorrupted images in the dataset (40 distinct standard deviations ranging from 0.01 to 0.60, for image pixel values between 0 and 1), and evaluated the average metric value on the dataset. We then accepted the Gaussian standard deviation as equivalent which achieved the nearest metric value on the dataset.

This process is illustrated in Fig. 5. We plot the empirical distributions of the averaged metric values for the 5 severity levels of the corruptions, as well as the averaged metric values for a subset of levels of additive Gaussian noise. The equivalent Gaussian noise levels for all of the corruptions in the dataset are plotted in Fig. 6.

Comparing the LPIPS Alex model with LPIPS Alex-lin, the latter of which has an additional linear layer trained supervisedly on human quality ratings, we note that the additional layer appears to increase relative sensitivity to independent noise and/or decrease sensitivity with respect to other types of distortions. This is evident from the Alex-lin curve being below the Alex curve in Fig. 6 on all distortions except the top three, and the corresponding histograms being shifted to the left in Fig. 5.

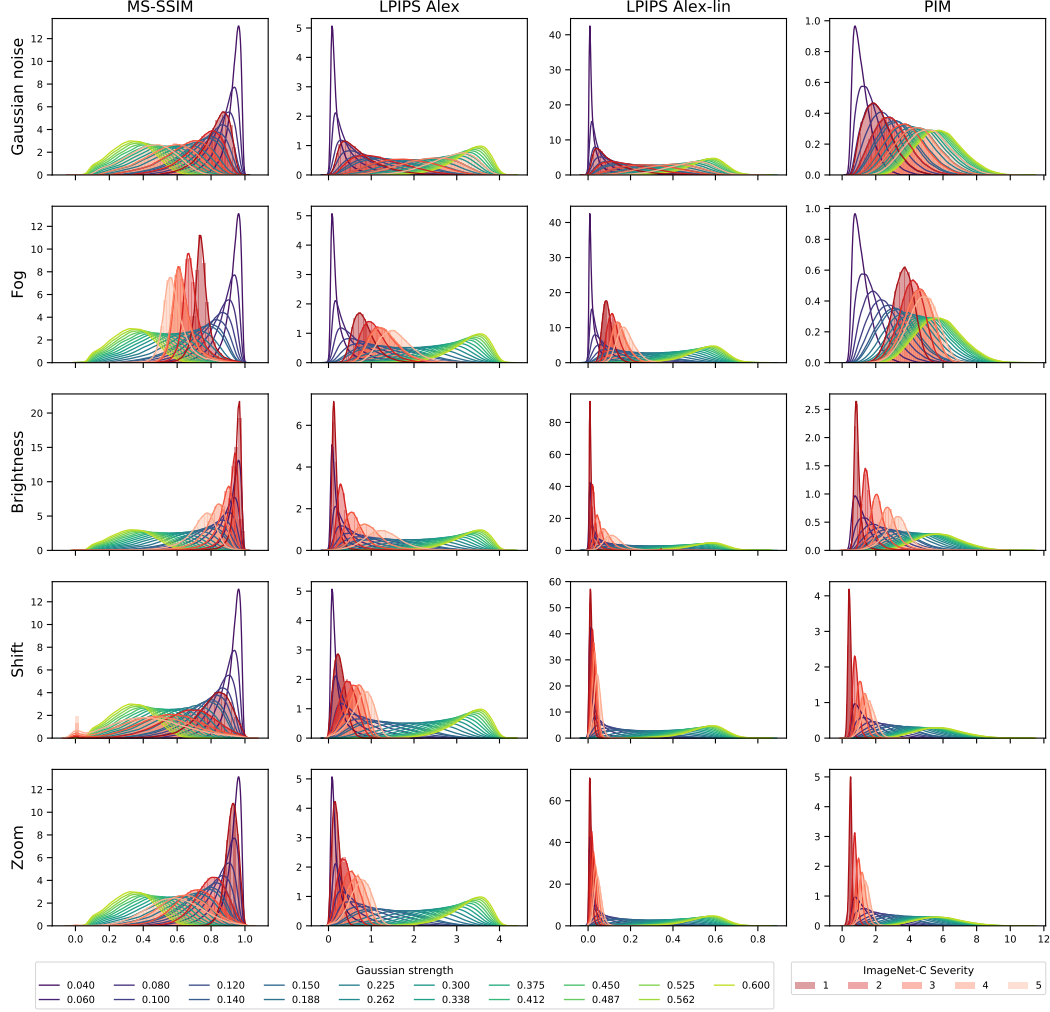


Figure 5: Histograms of metric values on the five different strengths of ImageNet-C corruptions (red) and a subset of Gaussian noise strengths (purple-green). The first row shows that the ImageNet-C Gaussian noise corruptions (with standard deviations of 0.08, 0.12, 0.18, 0.26, 0.38) exactly aligns with our additive Gaussian noise for all four models, indicating that the evaluation was correctly calibrated. The remaining rows reflect the same data visible in Figure 6 for these four selected corruptions, but giving additional information about the variance and skew of the empirical distributions of metric values. The abscissa reflects the scale of the corresponding metric; e.g., MS-SSIM ranges from 0 to 1, where 1 means the two images are identical, and 0 means the two images are maximally different. The other three models are Euclidean distances (i.e., 0 means that the images are identical). For MS-SSIM, the Shift transformation causes many images to saturate the score to 0, even with just a two pixel shift, making the empirical distributions bimodal. In contrast, the other three models are quite insensitive to the shifts and have more well-behaved empirical distributions.

More image examples are provided in Figs. 7 to 9. Fig. 7 provides more examples for the Fog and Zoom corruptions discussed in Section 3.3. The other two figures show the entire set of corruptions on the image shown in Fig. 3(b) and (c).

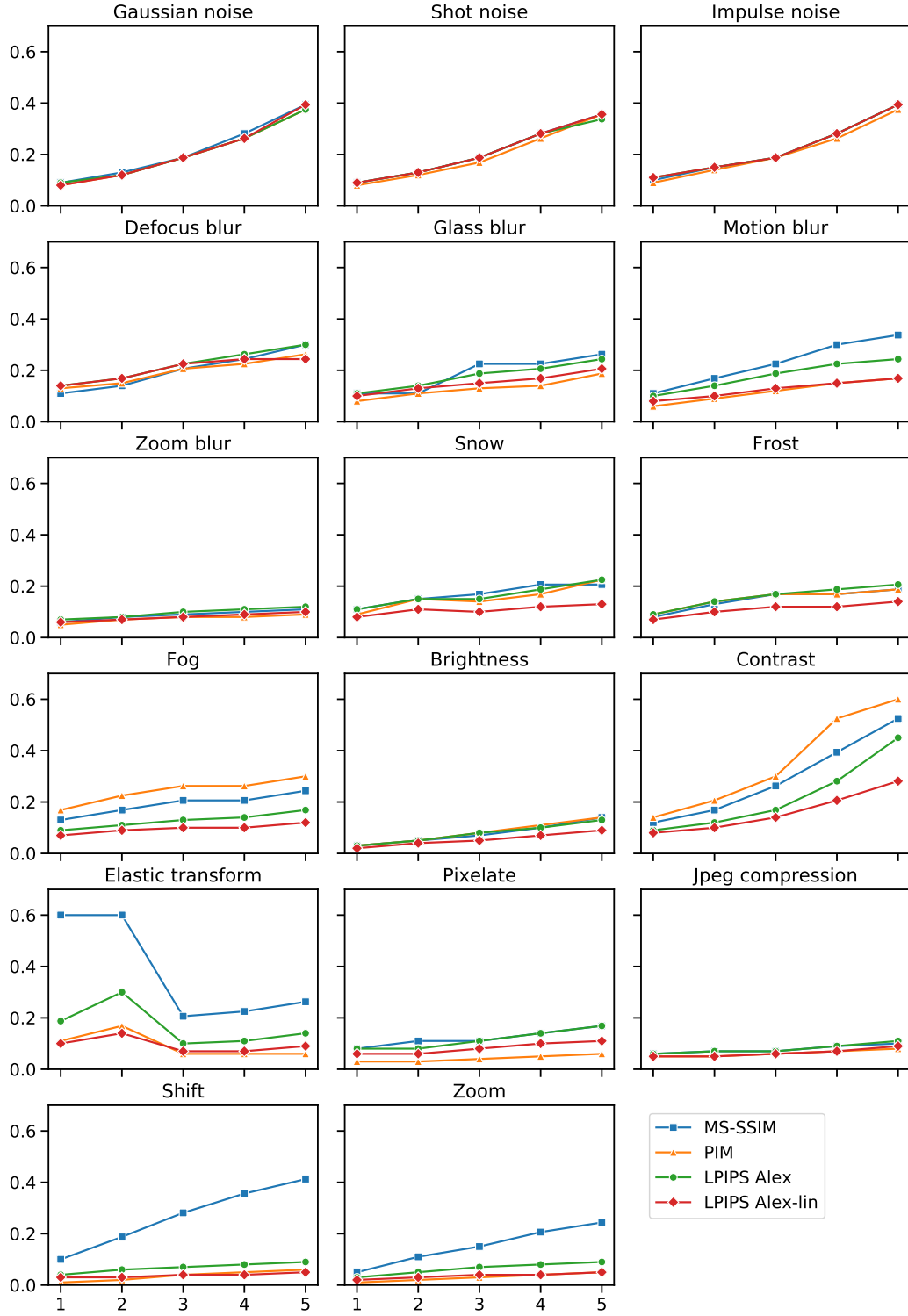


Figure 6: Same as Figure 3(a), but for all 15 ImageNet-C distortions, as well as our Shift and Zoom distortions.

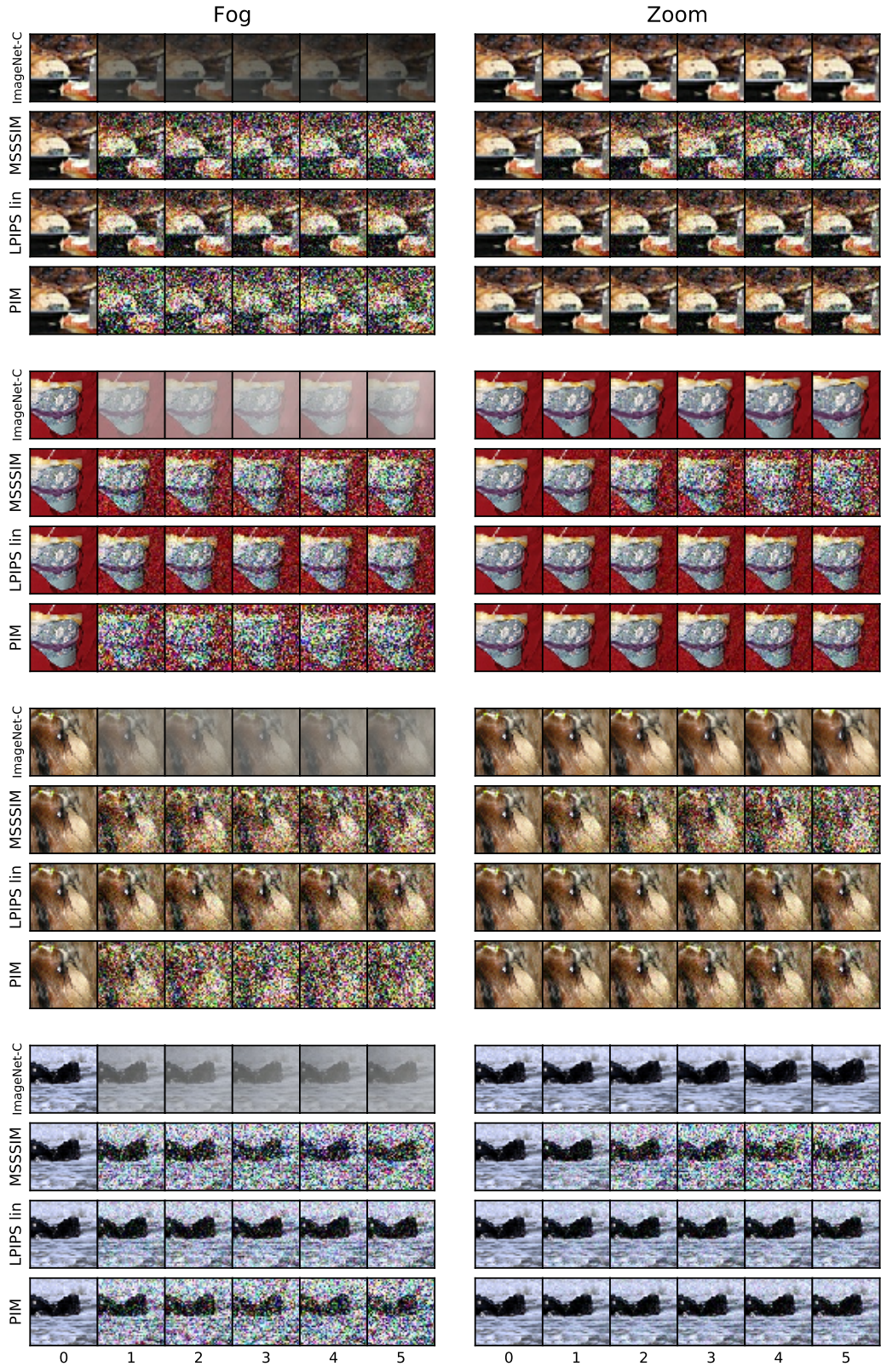


Figure 7: More examples of the Fog and Zoom corruptions discussed in Fig. 3.

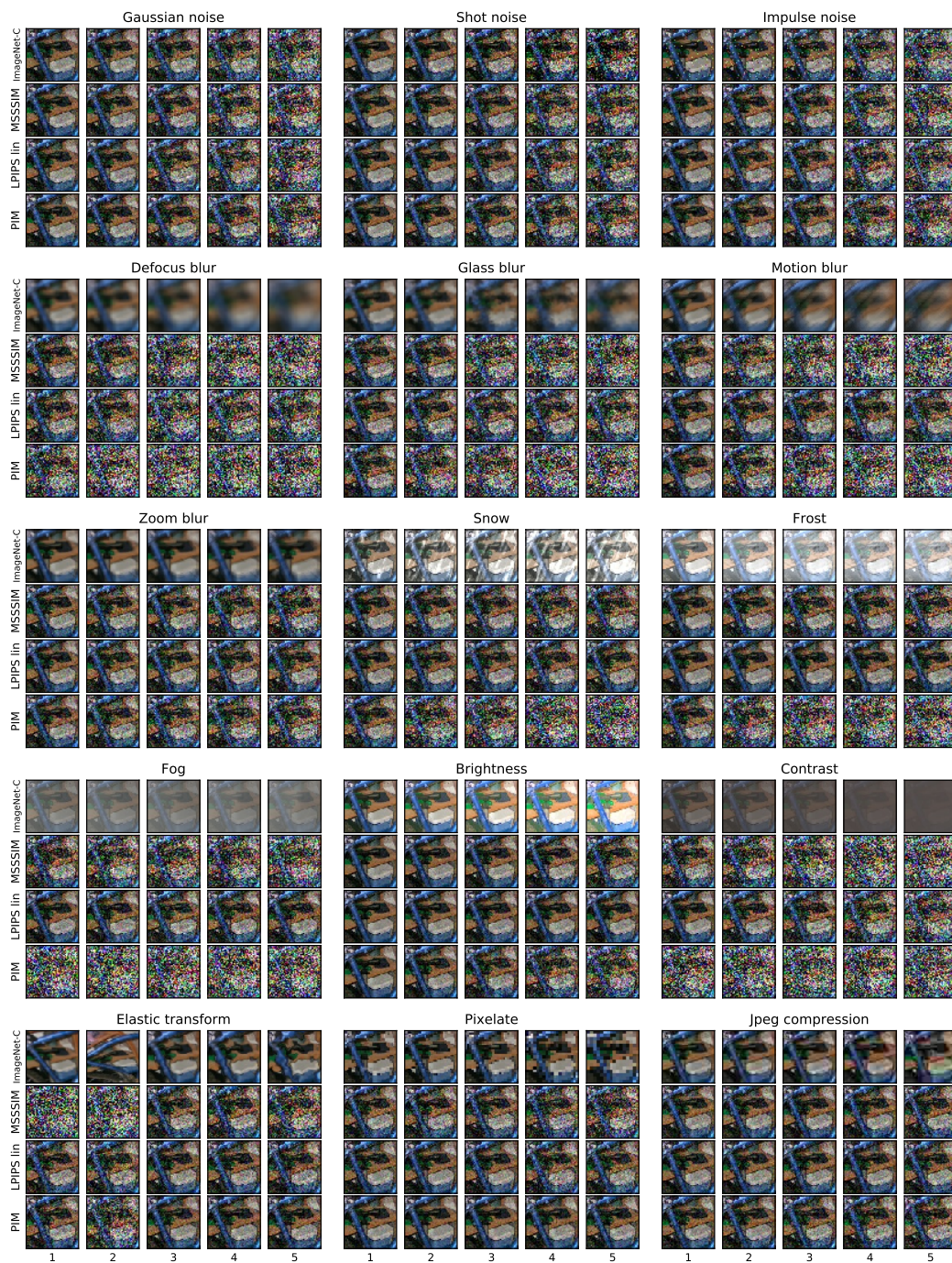


Figure 8: Visualization of all ImageNet-C corruptions with equivalent Gaussian strengths for the image in Fig. 3(b) and (c).

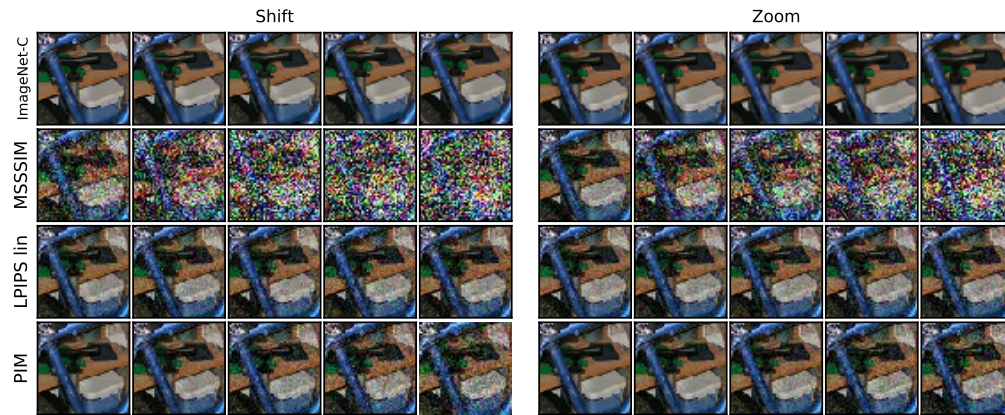


Figure 9: Visualization of our additional (Shift and Zoom) corruptions with equivalent Gaussian strengths for the image in Fig. 3(b) and (c).